

Downward and upward continuation of 2-D seismic data to eliminate ocean bottom topography's effect

Wang Xiang-Chun¹, Xia Chang-Liang², and Liu Xue-Wei¹

Abstract: In order to eliminate the effect of ocean bottom topography on seismic wave field, we transformed curved (x, z) coordinate system grids into rectangular (ξ, η) coordinate system grids and derived a 2-D scalar acoustic wave equation in the (ξ, η) domain. The seismic wave field collected at the sea surface was downward continued to the ocean bottom by the inverse finite difference method with the water velocity and then was reversely continued to the ocean surface by the finite difference method using the layer velocity from just below the ocean bottom in the (ξ, η) domain. Simulation calculations and practical application show that this method can not only remove the reflection travel time distortion but also correct the dynamic parameter changes caused by the ocean bottom topography. The inverted velocity after wave field continuation is much more accurate than before continuation and the image section was greatly improved compared to the original wave field.

Keywords: wave equation, continuation, ocean bottom topography, transformation

Introduction

Modern seismic exploration has entered into lithology exploration. In marine seismic exploration, the ocean bottom topography not only affects seismic imaging but also changes its dynamic parameters, resulting in poor seismic inversion accuracy. In order to eliminate these effects, we transformed curved (x, z) coordinate system grids into rectangular (ξ, η) coordinate system grids and derived a 2-D scalar acoustic wave equation in the (ξ, η) coordinate system. First, the original seismic wave field is downward continued to the ocean bottom boundary using the inverse finite difference method and then upward continued to the ocean surface by the finite difference method. During downward continuation we use the water velocity and upward continue using the

interval velocity beneath the ocean bottom.

In this paper, we designed two geological models: one having a water layer with ocean bottom topography and another model without a water layer. Using the derived wave-equation we simulated multiple shot gathers for the two models and then the modeled seismic wave fields were processed by our continuation method. The reflection travel time of the horizontal reflection layer (HRL) before and after the continuations, the HRL reflection travel time without the sea water layer, and their maximum amplitude values are analyzed and AVO velocity inversion was performed for the CMP gathers. The inverted velocity precision of the three wave fields was compared. Finally, we processed real marine seismic data, compared the differences between the original and continued seismic wave field of the shot and CMP gathers, and analyzed the effects of seismic wave field

Manuscript received by the Editor November 13, 2009; revised manuscript received March 22, 2010.

This research is sponsored by the National 973 Program of China (Grant No. 2009CB219505) and International Science & Technology Cooperation Program of China (Grant No. 2010DFA21630).

1. Key Laboratory of Geo-detection (China University of Geosciences, Beijing), Ministry of Education, Beijing 100083, China.

2. Overseas Business Department of Geophysical Research Institute, BGP of CNPC, Zhuozhou 072750, China.

Downward and upward continuation

continuations on seismic imaging.

Currently, grid transformation methods are mainly applied in forward seismic modeling. Tessmer et al. (1992), Hestholm and Ruud (1998), and Hestholm (2003) simulated the wave fields using transformation methods. The procedures were: First, transform the curved (x, z) coordinate system grids into rectangular (ξ, η) coordinate system grids, then derive the elastic wave equation in the transformed coordinate system, and finally simulate the seismic wave field using the corresponding method. Most of them obtained satisfactory results.

This problem can also be solved by the Kirchhoff integral method but is accompanied by seismic waveform distortion. Here we use this method to process marine seismic data. As a result, not only the ocean bottom topography effect on the seismic wave field was removed but also artificial noise diffractions caused by continuation in the irregular grid of the original coordinate system was suppressed. It is because that the rectangular (ξ, η) coordinate system grids are regular that the diffraction noise disappears. There is also no waveform distortion.

Grid transformations and the 2-D scalar wave equation derivation in the ξ, η domain

For the 2D case, curved (x, z) coordinate system grids are mapped into rectangular (ξ, η) coordinate system grids. The rectangular grids in the ξ, η domain are limited by $\xi=0$, $\xi=\xi_{\max}$, $\eta=0$, and $\eta=\eta_{\max}$ (Tessmer et al., 1992; Fornberg, 1998; Nielsen and Skovgaard, 1994). The curved grids in the x, z domain are limited by $x=0$, $x=x_{\max}$, $z=0$, and $z=z_0(\xi)$. Here a simple linear relationship is adapted for grid transformation from

curved into rectangular grids (Hestholm and Ruud, 1994 and 1998; Bevc, 1997) as:

$$\begin{cases} \xi(x, z) = x \\ \eta(x, z) = \frac{z\eta_{\max}}{z_0(\xi)}, \end{cases} \quad (1)$$

where x is a function of ξ , z is a function of ξ and η , and $z_0(\xi)$ is a function to describe the ocean bottom topography. When the ocean water depth to which all the receiver points are known, the $z_0(\xi)$ value of any point can be calculated using a three-term spline interpolation. The mapping relationship sketch is shown in Figure 1.

Using equation (1), we derive the spatial derivative of seismic wave field for the x and z directions as:

$$\begin{cases} \frac{\partial^2 u}{\partial x^2} = \frac{\partial^2 u}{\partial \xi^2} + 2.0 \frac{\partial^2 u}{\partial \xi \partial \eta} \frac{\partial \eta}{\partial x} + \frac{\partial u}{\partial \eta} \frac{\partial^2 \eta}{\partial x^2} + (\frac{\partial \eta}{\partial x})^2 \frac{\partial^2 u}{\partial \eta^2}, \\ \frac{\partial^2 u}{\partial z^2} = (\frac{\partial \eta}{\partial z})^2 \frac{\partial^2 u}{\partial \eta^2} \end{cases}, \quad (2)$$

where $u=u(\xi, \eta, t)$ represents the seismic wave field at (ξ, η) . The values of $\partial \xi / \partial x$, and $\partial \eta / \partial x$ can be calculated by the following equation (Nielsen and Skovgaard, 1994; Hestholm and Ruud, 1994 and 1998):

$$\begin{cases} \frac{\partial \xi}{\partial x} = 1, \\ \frac{\partial \xi}{\partial z} = 0, \\ \frac{\partial \eta}{\partial x} = -\frac{\partial z}{\partial \xi} / \frac{\partial z}{\partial \eta} = -\frac{\partial z_0(\xi)}{\partial \xi} \frac{\eta}{z_0(\xi)}, \\ \frac{\partial \eta}{\partial z} = \frac{\partial x}{\partial \xi} / \frac{\partial z}{\partial \eta} = \frac{\eta_{\max}}{z_0(\xi)}. \end{cases} \quad (3)$$

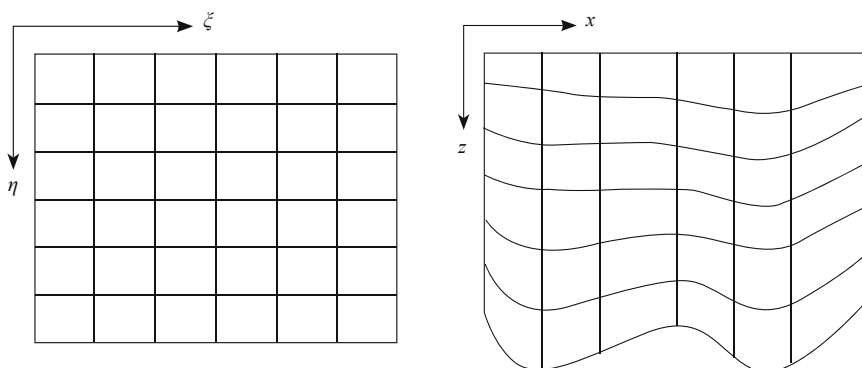


Fig. 1 Transformation relationship between the rectangular and curved grids.

The 2-D scalar acoustic wave equation in the (x, z) coordinate system is

$$\frac{\partial^2 u}{\partial x^2} + \frac{\partial^2 u}{\partial z^2} = \frac{1}{v^2} \frac{\partial^2 u}{\partial t^2}, \quad (4)$$

Based on equation (2), we can transform the (x, z) coordinate system into the (ξ, η) coordinate system and equation (4) can be rewritten as:

$$\begin{aligned} & \frac{\partial^2 u}{\partial \xi^2} + 2 \frac{\partial^2 u}{\partial \xi \partial \eta} \frac{\partial \eta}{\partial x} + \frac{\partial^2 u}{\partial \eta^2} \left(\frac{\partial \eta}{\partial x} \right)^2 \\ & + \frac{\partial u}{\partial \eta} \frac{\partial^2 \eta}{\partial x^2} + \left(\frac{\partial \eta}{\partial z} \right)^2 \frac{\partial^2 u}{\partial \eta^2} = \frac{1}{v^2} \frac{\partial^2 u}{\partial t^2}, \end{aligned} \quad (5)$$

Assuming $\partial \eta / \partial x = c_1$, $\partial \eta / \partial z = c_2$, and $\partial^2 \eta / \partial x^2 = c_3$, c_3 can be expressed as

$$c_3 = \frac{\partial^2 \eta}{\partial x^2} = - \frac{\partial^2 z_0(\xi)}{\partial \xi^2} \frac{\eta}{z_0(\xi)} + 2.0 \cdot \left[\frac{\partial z_0(\xi)}{\partial \xi} \right]^2 \frac{\eta}{[z_0(\xi)]^2}, \quad (6)$$

Thus equation (5) can be simplified to

$$\begin{aligned} & \frac{\partial^2 u}{\partial \xi^2} + 2c_1 \frac{\partial^2 u}{\partial \xi \partial \eta} + (c_1^2 + c_2^2) \frac{\partial^2 u}{\partial \eta^2} + \frac{\partial u}{\partial \eta} c_3 \\ & = \frac{1}{v^2} \frac{\partial^2 u}{\partial t^2}, \end{aligned} \quad (7)$$

Model calculation and analysis

Two geological models (A) and (B) are established with the interval velocities and layer depths shown in Figure 2. For the forward modeling, there are 260 shots in each model with shot spacing of 20 m and 600 receivers in each shot which are distributed on the model surface with 10 m spacing. The horizontal layer (HL) seismic wave fields before and after continuations between layers V2 and V3 in Model A are analyzed and compared to the HL seismic wave fields between V2 and V3 in Model B. Theoretically, the wave fields of Model A after continuation should be the same as the wave fields of Model B.

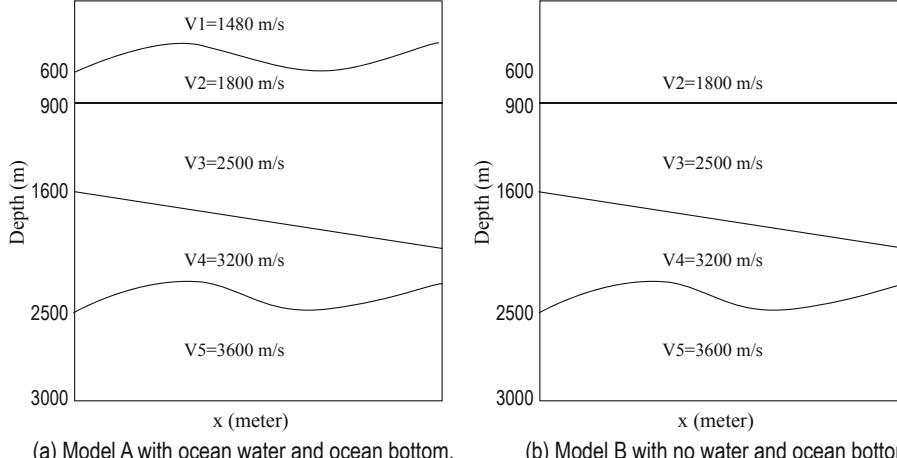


Fig. 2 Two geological models with layer velocities and depths.

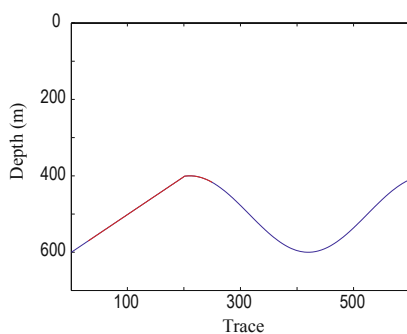


Fig. 3 The analyzed area (red) of the 50th shot in the geological model.
(The x-axis is trace number and the y-axis the water depth)

Comparison of shot gathers before and after continuation

The red curve in Figure 3 indicates the 50th shot's analysis location. Figure 4 shows the HL reflection beneath the ocean bottom in the analyzed region (Model A). Figure 5 shows the results after forward and reverse continuation of the seismic wave fields shown in Figure 4.

The shot is located at the center of the analyzed area. If the ocean bottom is horizontal, the time-distance

Downward and upward continuation

curve reflected from the HL beneath the ocean bottom should be a hyperbola symmetrical to the shot point. However, the ocean bottom topography makes the curve asymmetric. The travel time on the left side is

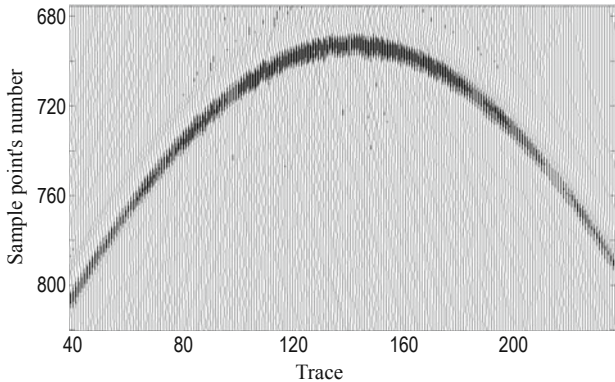


Fig. 4 The 50th shot's HL layer seismic reflection for Model A.

Figure 6 is the HL's reflection travel time curves before continuation (red) and after continuation (yellow) (Model A) and without ocean water and ocean bottom (blue) (Model B). From the figure we see that the HL's reflection travel time after continuation is consistent with the layer from Model B. This demonstrates that our method can remove the ocean bottom topography effect on the reflection travel times from below the ocean bottom.

Figure 7 displays that ocean bottom topography also

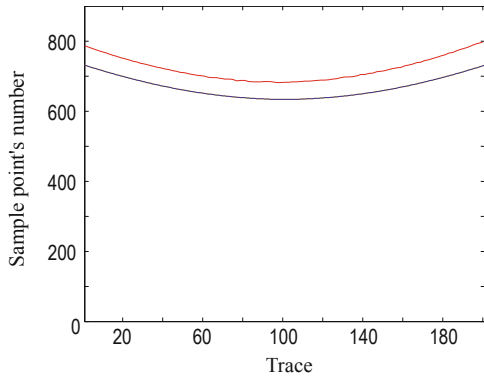


Fig. 6 Travel time curve from Model A before continuation (red) and after continuation (yellow) and from Model B without the ocean layer (blue).

Analysis of CMP gathers before and after continuation

The simulated shot gathers are sorted to CMP gathers for analysis. The red curve in Figure 8 indicates the location of the 200th CMP gather. The CMP point

greater than the right side because the ocean bottom on the left side is deeper than the right side. The continued wave field is symmetric with respect to the shot (see Figure 5).

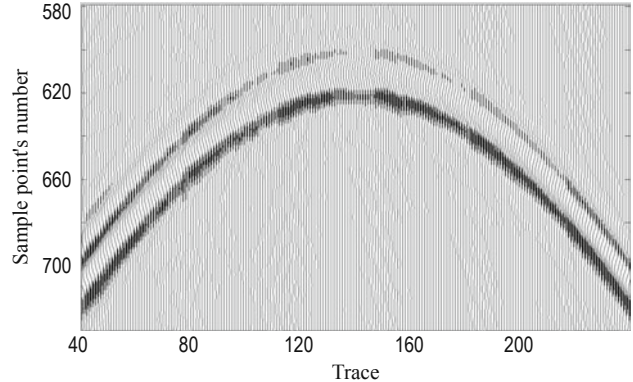


Fig. 5 Model A HL layer seismic reflection after continuation.

has an effect on the reflection amplitudes beneath the ocean bottom and the effect increases with the offset. In this case, the reflection amplitude changes about 11% at 1000 m offset. The reflection amplitude curve after forward and reverse continuations (Model A) is similar to the amplitudes from Model B without the ocean layer, which confirms our continuation method can at least partially correct the amplitude distortion caused by the ocean bottom topography.

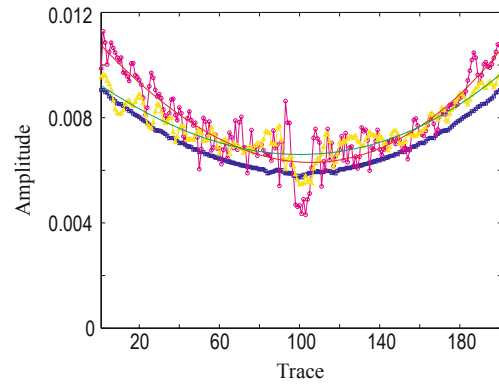


Fig. 7 The maximum amplitude curves before continuation (purple), after continuation (yellow), and without the ocean layer (blue). The red curve is fit to the purple curve and the green curve is fit to the yellow curve.

lies in the middle of the analyzed area. Figure 9 is the modeled HL's seismic reflection beneath the ocean bottom in the analysis region from Model A. Figure 10 is the results after forward and reverse continuation of the seismic wave field in Figure 9. Figure 11 is the HL's reflection travel time curve before (red) and after

(yellow) continuation (Model A) and no ocean layer (blue) (Model B). Figure 12 is the HL's reflection maximum amplitude curves before (purple) and after (yellow) continuations (Model A) and without ocean layer (blue) (Model B). The red curve is fit to the purple curve and the green curve is fit to the yellow curve.

By analyzing the CMP gathers we conclude that the ocean bottom topography not only distorts the HL's reflection travel times beneath the ocean bottom but also affects the AVO. These effects can be corrected by the forward and reverse time continuation.

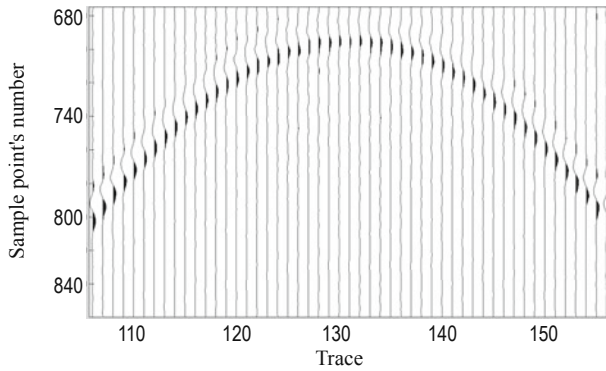


Fig. 9 The 200th CMP gather's simulated seismic reflection wave field from Model A

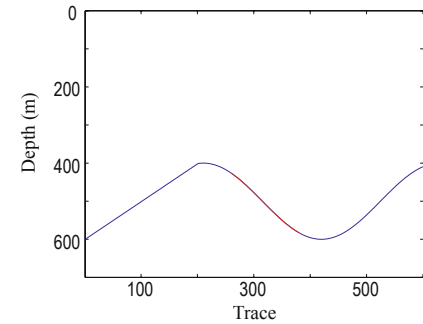


Fig. 8 200th CMP gather analysis area (red) in the complete geological model. The x-axis is the trace number and the y-axis is the water depth.

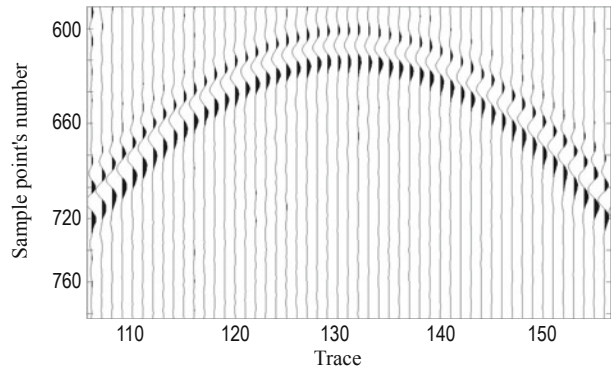


Fig. 10 Seismic wave field from Figure 9 after continuation.

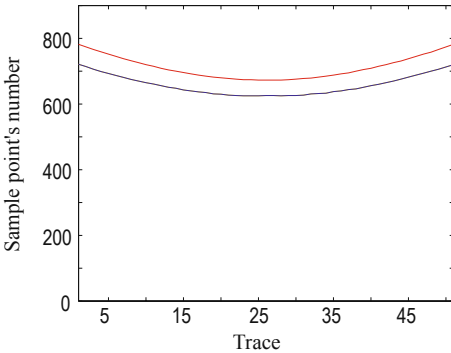


Fig. 11 Travel time curves before continuation (red) and after continuation (yellow) for Model A and without the ocean layer (blue) of Model B.

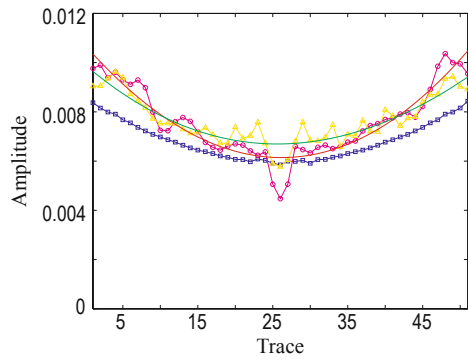


Fig. 12 The maximum amplitudes curves before continuation (red), after continuation (green), and without the ocean layer (blue).

Precision of velocity inversion before and after the continuations

AVO inversion is one of the main techniques to obtain P- and S- wave velocities and the results of AVO inversion can be used to predict gas hydrates and detect oil and gas. The ocean bottom topography affects the variation of amplitude with offset and so it influences the AVO inversion results. Now we analyze the effect of ocean bottom topography on AVO inversion accuracy by

numerical modeling.

We use the 200th CMP's reflection amplitude curves for P wave velocity inversion. When V2 is given, for inverting V3 of Model A the inverted velocity is 2682 m/s before and 2536 m/s after continuation. For inverted V3 of Model B the velocity is 2508 m/s. Compared with the models' real velocity (2500 m/s), their errors are 7.28%, 1.44%, and 0.33%. When V3 is given, for inverting V2 of Model A, the inverted velocity is 1677 m/s before and 1774 m/s after continuation. For V2 of the

Downward and upward continuation

Model B, the velocity is 1794 m/s. Comparing with the models' real velocity (1800 m/s), their errors are 6.81%, 1.44%, and 0.33%.

In the region that this CMP gather covers, the maximum angle of ocean bottom topography is about 14 degrees. At 125-meter offset, the amplitude change caused by the bottom topography is about 25%. Compared to the case without the ocean layer, the effect of ocean bottom on AVO inversion is that the accuracy of AVO inversion decreases 6.95% (i.e., 7.28% - 0.03%). This amount of error is not acceptable for lithology exploration.

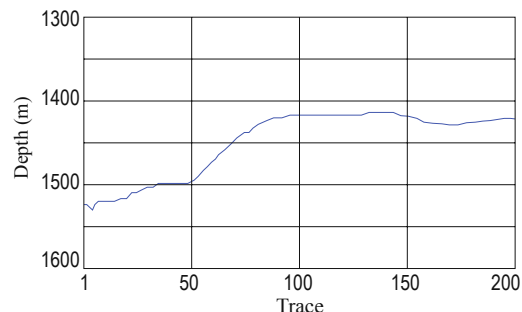


Fig. 13 Water depth at shot gather 1270.

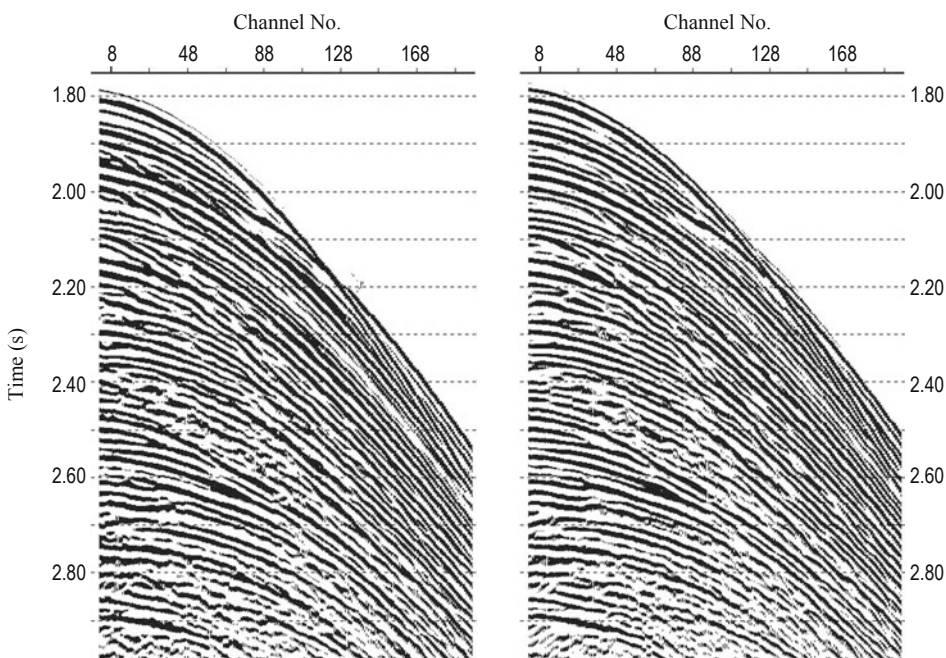


Fig. 14 Shot gather 1270 before continuation (left) and after continuation (right).

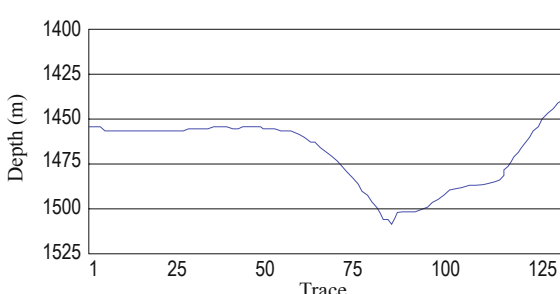


Fig. 15 Water depth at CDP gather 2379.

In this example, the velocity inversion results tell us that the effect of bottom topography is eliminated by using our continuation technique. The AVO velocity inversion accuracy is increased by 5.84% (i.e., 7.28% - 1.44%).

From the AVO inversion we can not only obtain

the P wave velocity but also S wave velocity, Lamé parameters, and so on. We did not study the ocean bottom topography effect on these parameters.

Application example

We processed real 2D marine seismic data from a deep-water area in the South China Sea using our continuation method. There are 400 shots on this line with a shot spacing of 25 m and there are 480 receivers in each shot gather with a receiver spacing of 12.5 m. The time sample interval is 1 ms. Figure 13 shows the ocean bottom depth corresponding to each geophone position for shot gather 1270. At near offsets the oceanic bottom is deeper than at the far offsets and the depth varies quickly. Figure 14 is a comparison

of the shot gather data before continuation (left) and after continuation (right). We can see that the reflection travel time was greatly affected because of quickly varying oceanic bottom topography at near offsets. Reflection events are more continuous, the distortions disappear, and the reflection wave forms are more

consistent with each other after continuation. Figure 15 shows the water depths at the geophone positions of CDP gather 2379. Figure 16 shows the CMP gather wave fields before continuation (left) and after continuation (right); the events are more continuous and some noise disappears.

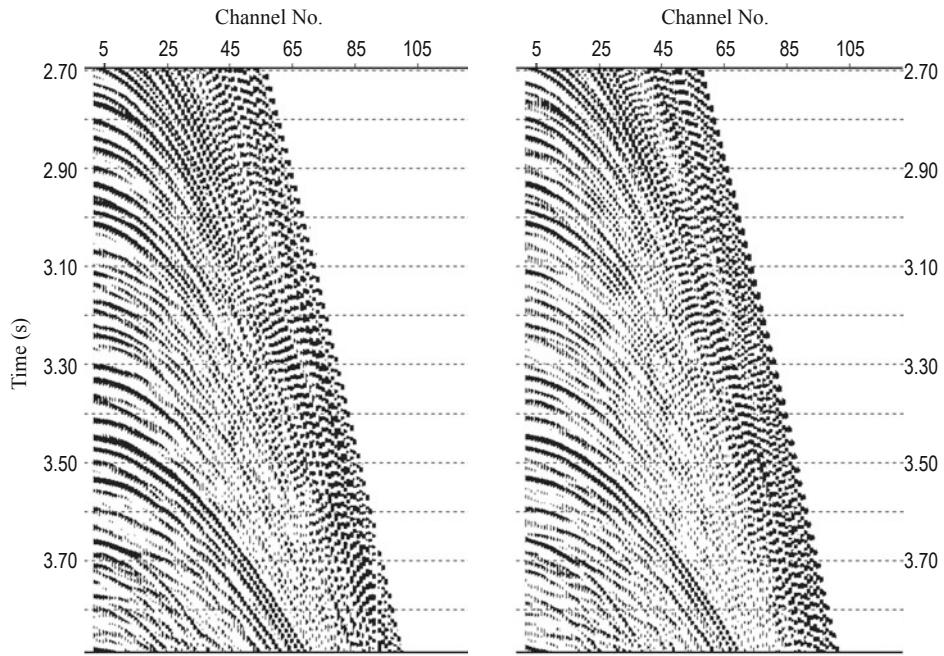


Fig. 16 CMP gather 2379 before continuation (left) and after continuation (right)

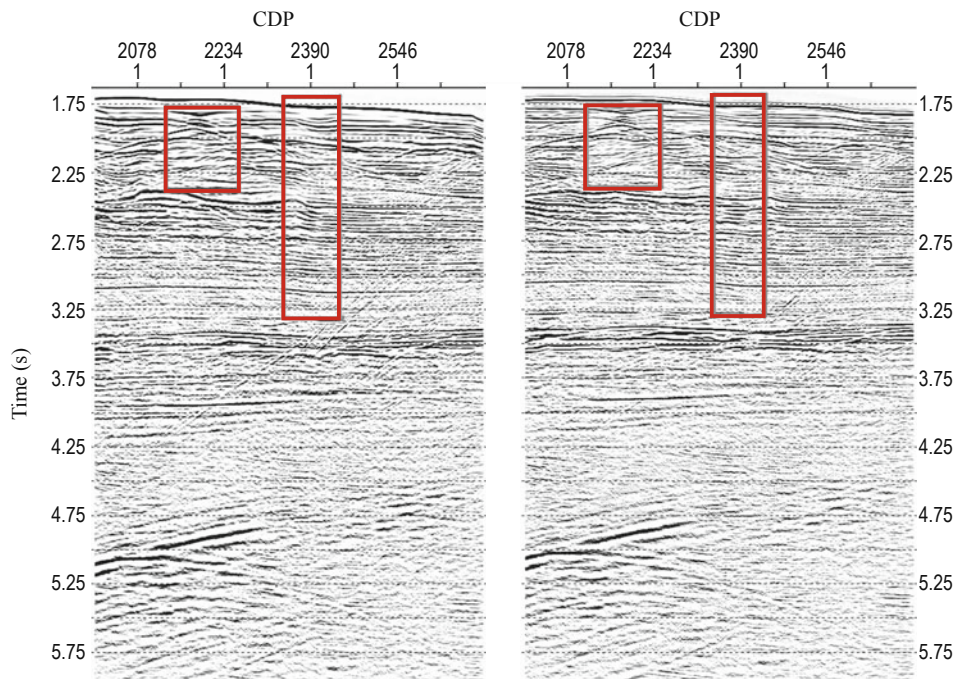


Fig. 17 Stack sections before continuation (a) and after continuation (b).

Downward and upward continuation

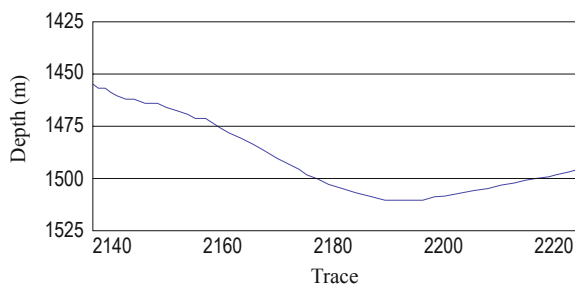


Fig. 18 Water depth in the left red block in Figures 17a and 17b.

Figure 17 shows the stack sections before continuation and after continuation. Figure 18 is the water depths of the left red block of Figure 17a. From this figure we can see that the bottom topography changes quickly

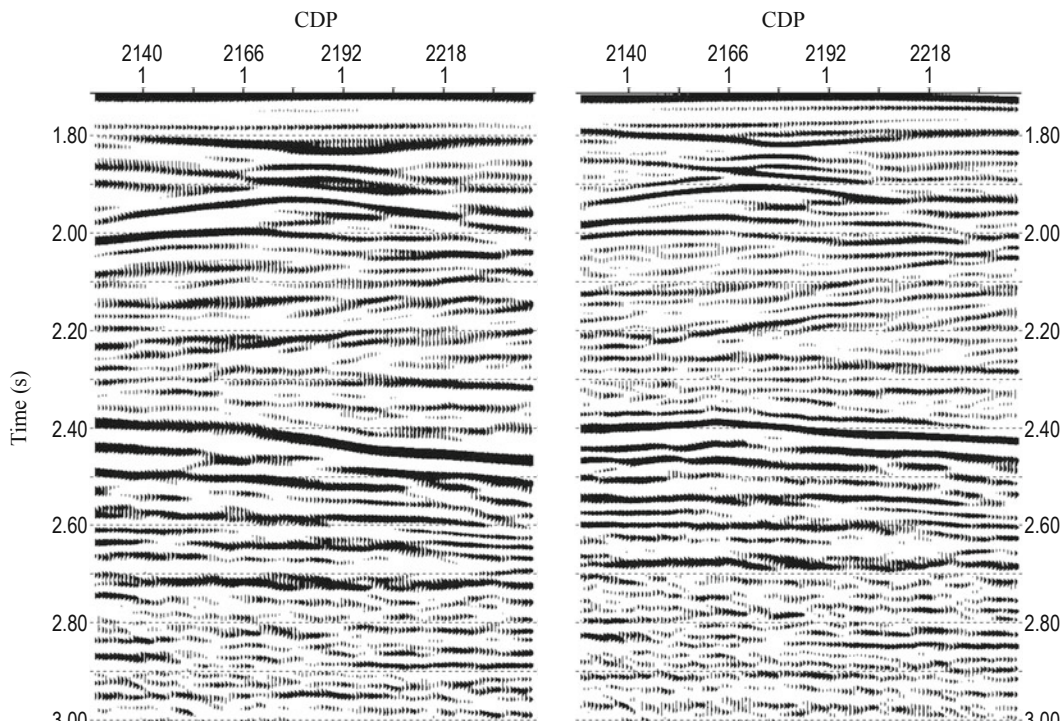


Fig. 19 The zoomed stack sections of the left red blocks in the Figures 17 a and 17b.

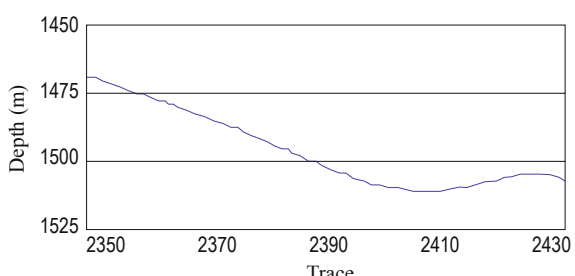


Fig. 20 Water depth in the right red block of Figures 17a and 17b.

and is deeper at the left than at the right. Figure 19 is the zoomed section of the left red block in Figure 17. Because the continuation eliminates the effects of the oceanic bottom topography on the reflections, the effect of horizontal velocity variation on seismic imaging is reduced, subsequent processes are more precise, and the final stack section's resolution is higher (see near 1.85 s in Figure 19). The location and the relations of the reflections are clearer between 2.4 and 2.7 s in Figure 19, the events are more continuous and smooth, and the S/N ratio improves. Figure 20 is the water depth in the right red block of Figure 17a. Figure 21 is the zoomed sections of the right red block with and without continuation. From this zoomed section we can see that the quality of the stack section after continuation is better than before continuation.

Conclusions

Model calculations and analysis show that the ocean bottom topography not only distorts the reflection travel time but also greatly affects AVO attributes. The continuation method applied in this paper not only eliminates the reflection travel time changes but also corrects the dynamic distortion. The ocean bottom topography also affects the precision of AVO velocity inversion, which can be improved by continuation.

The real marine seismic data processing indicates that the continuation method eliminates the travel time distortion, so the imaging quality obviously improves. Because the continuation used here is based on the wave

equation method and the wave propagation conforms to the equation, this method can correct the kinematic and dynamic distortion caused by the ocean bottom topography.

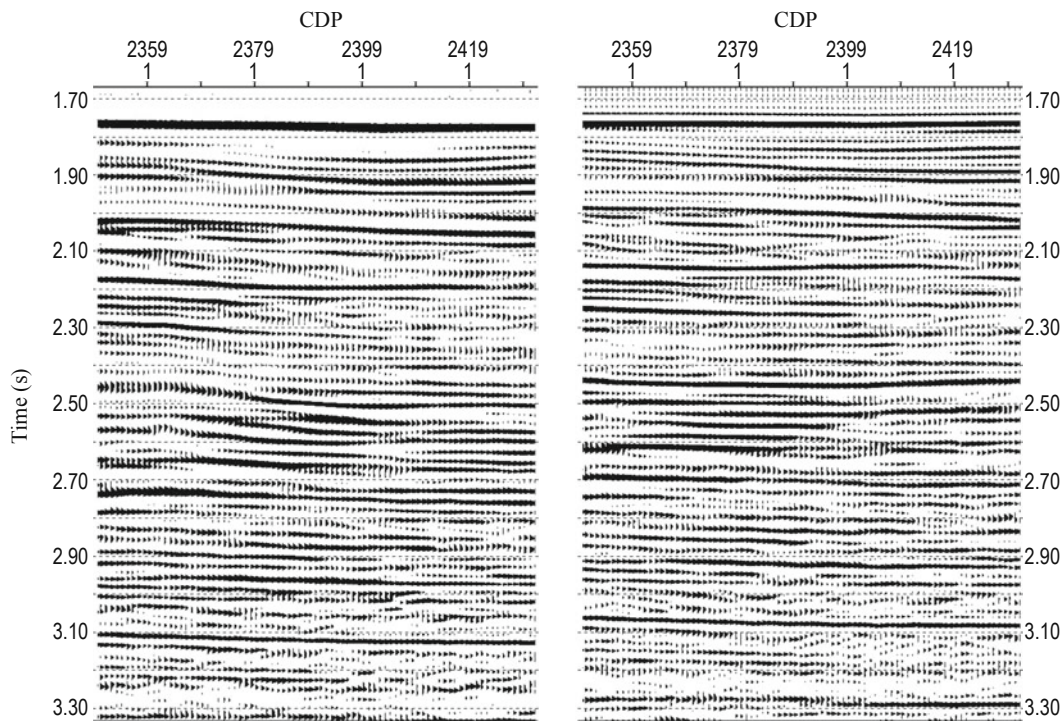


Fig. 21 The zoomed stack sections of the right red blocks of Figures 17a and 17b.

The ocean bottom topography effect on other AVO inversion parameters (shear wave velocity, Lamé parameters, and so on) and its accuracy improvement after continuation should be studied in the future.

The shortcoming of this method is the frequency dispersion effects caused by the discreteness of the wave equation and many scholars (Liu et al., 1998) have studied this problem.

References

- Ai, Y. S., and Zheng, T. Y., 1998, Wavefield continuation depth filtering: Chinese Journal of Geophysics, **41**(3), 400 – 407.
- Berryhill, J. R., 1979, Wave-equation datuming: Geophysics, **44**(8), 1329 – 1344.
- Bevc, D., 1997, Flooding the topography; wave equation datuming of land data with rugged acquisition topography: Geophysics, **62**(5), 1558 – 1569.
- Fornberg, B., 1998, The pseudospectral method: Accurate representation of interfaces in elastic wave calculations:

- Geophysics, **53**(5), 625 – 637.
- Hestholm, S., and Ruud, B., 1994, 2D finite-difference elastic wave modeling including surface topography: Geophysical Prospecting, **42**, 371 – 390.
- Hestholm, S., and Ruud, B., 1998, 3-D finite-difference elastic wave modeling including surface topography: Geophysics, **63**(2), 613 – 622.
- Liu, Y., Li, C.C., and Mou, Y.G., 1998, Finite-difference numerical modeling of any even-order accuracy, Oil Geophysics Prospecting, **33**(1), 1 – 10.
- Nielsen, P., and Skovgaard, O., 1994, Using the pseudospectral technique on curved grids for 2D acoustic forward modeling: Geophysical Prospecting, **42**, 321 – 341.
- Tessmer, E., Kosloff, D., and Behle, A., 1992, Elastic wave propagation simulation in the presence of surface topography: Geophysics. J. Int., **108**, 621 – 632.

Wang Xiang-Chun: See biography and photo in the Applied Geophysics March 2009 issue, P. 15